JACS
JOURNAL OF THE AMERICAN CHEMICAL SOCIETY
Article
pubs.acs.org/JACS

Synthesis and Crystallographic Analysis of Shape-Controlled SnS Nanocrystal Photocatalysts: Evidence for a Pseudotetragonal Structural Modification

Adam J. Biacchi,[†] Dimitri D. Vaughn II,[†] and Raymond E. Schaak*

Department of Chemistry and Materials Research Institute, The Pennsylvania State University, University Park, Pennsylvania 16802, United States

Supporting Information

ABSTRACT: Tin sulfide, SnS, is a narrow band gap semiconductor comprised of inexpensive, earth abundant, and environmentally benign elements that is emerging as an important material for a diverse range of applications in solar energy conversion, energy storage, and electronics. Relative to many comparable systems, much less is known about the factors that influence the synthesis or morphology-dependent properties of SnS nanostructures. Here, we report the synthesis of colloidal SnS cubes, spherical polyhedra, and sheets and demonstrate their activity for the photocatalytic degradation of methylene blue. We also study their morphology-dependent polymorphism using an in-depth crystallographic analysis that correlates high-resolution TEM data of individual nanocrystals with ensemble-based electron diffraction and powder XRD data. These studies reveal that the crystal structure adopted by the SnS cubes and spherical polyhedra is expanded along the *a* and *b* axes and contracted along *c*, converging on a pseudotetragonal cell that is distinct from that of orthorhombic α-SnS, the most stable polymorph. All of the peaks observed in powder XRD patterns that are often interpreted as originating from a mixture of metastable zincblende-type SnS and α-SnS can instead be accounted for by this single-phase pseudotetragonal modification, and this helps to rationalize discrepancies that exist between theoretical predictions of SnS polymorph stability and interpretations of experimental diffraction data. This same crystallographic analysis also indicates the morphologies of the nanocrystals and the facets by which they are bound, and it reveals that the SnS cubes form through selective overgrowth of spherical polyhedral seeds.

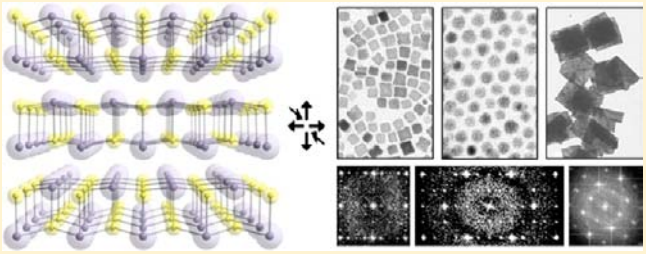

INTRODUCTION

Among the most widely studied semiconductor nanocrystals are PbS, PbSe, CdS, and CdSe, which have desirable and tunable optoelectronic properties distinct from those found in the bulk materials[1−3] but include highly toxic lead and cadmium. Compounds of tin with group VI elements such as sulfur represent promising and more benign alternatives that contain exclusively inexpensive and earth-abundant elements.[4] In particular, tin(II) sulfide (SnS), which occurs naturally as the mineral herzenbergite, has gained increasing attention. Bulk SnS is a p-type semiconductor with an indirect band gap of 1.07 eV and a direct band gap of 1.3 eV that exhibits a high absorption coefficient and excellent hole mobility.[5,6] Additionally, the exciton Bohr radius of SnS is estimated to be ∼7 nm, such that the band gap of SnS can increase for particles with diameters on the order of 14 nm or less due to quantum confinement effects.[7−9] The similarity of its indirect band gap to that of silicon, coupled with its proximity to the band gap of optimum photovoltaic efficiency according to the Shockley−Quesser limit, has generated much interest in applying SnS toward devices such as solar cells,[10] field effect transistors,[11] photodetectors,[12] and electrochemical capacitors,[13] as well as Li ion battery anodes[14] and photocatalysts.[15]

SnS typically crystallizes in the GeS structure type, which is orthorhombic (*Pnma*) and can be described as a strongly distorted NaCl structure with nominally octahedral coordination geometry.[16] Two-atom-thick Sn−S layers extend in the *b*- and *c*-directions, while the interlayer bonding, extending in the *a*-direction to connect the Sn−S slabs, is weaker.[17] These bonding characteristics, therefore, impart anisotropy on the structure of GeS-type SnS by providing a chemical driving force for SnS crystallites to adopt two-dimensional (2D) morphologies, including nanosheets, nanoplates, and nanobelts. The SnS(100) surface is selectively exposed in these nanostructures and is relatively inert due to a lack of dangling bonds.[18] The layered structure also leads to strongly anisotropic physical properties, which makes the fabrication of morphologically diverse structures particularly interesting. While less studied than its other IV−VI nanocrystal counterparts, a growing number of reports describe the synthesis, properties, and applications of monodisperse colloidal SnS nanostructures. Using solution-based methods, there are reports of ∼20 nm plates,[19] ∼10 nm triangular particles,[20] and ∼500 nm

Received: May 23, 2013
Published: July 3, 2013

   dx.doi.org/10.1021/ja405203e | J. Am. Chem. Soc. 2013, 135, 11634−11644

tetrahedra.[19,21] However, the majority of synthetic protocols that produce colloidal SnS yield roughly spherical or irregular particles.[8,11,20−24]

Three key observations emerge from the existing reports of SnS nanostructures. First, while a few examples of high-quality colloidal SnS nanocrystals have been reported, much less is known about the chemical factors that influence their synthesis than for other, more highly studied colloidal semiconductor systems. Second, the colloidal SnS nanocrystal system lacks the rigorous morphological diversity and general size and shape uniformity that is becoming increasingly common for other related cadmium and lead chalcogenides. The accessibility of high-quality shape-controlled colloidal semiconductor nanocrystals with excellent and useful properties is an important prerequisite for incorporation into emerging applications and next-generation technologies. Third, a growing number of SnS nanocrystal reports describe them as adopting a mixture of the standard GeS-type phase that is stable in bulk systems, along with a metastable zincblende (ZB) polymorph that is not observed in bulk SnS. This highlights the potentially complex structural diversity that exists in nanoscopic SnS.

The metastable ZB polymorph that has been reported in syntheses of both SnS thin films[25−28] and colloidal nanoparticles[11,19,21,29] is important because the different arrangement of atoms would lead to physical, optoelectronic, and catalytic properties that are distinct from those of GeS-type SnS, which is also referred to as α-SnS. However, to our knowledge, phase-pure ZB-type SnS has not been reported for SnS, in either the colloidal or thin film literature. Careful analysis of the published powder X-ray diffraction patterns from all recent reports indicate that the proposed metastable ZB-type SnS phase can account for only some of the observed reflections, with the remaining peaks attributed to the GeS-type phase (α-SnS). Walsh and co-workers used density functional theory (DFT) calculations to study the stability of ZB-type SnS relative to other polymorphs. Interestingly, they concluded that the formation of ZB-type SnS is not feasible on the basis of thermodynamic arguments and that prior reports of its formation may be inaccurate because of misinterpreted powder XRD data.[30] This, coupled with the fact that colloidal nanoparticles of high-purity ZB-type SnS have not been reported, warrants more in-depth investigations of the crystal structure adopted by SnS when synthesized as colloidal nanoparticles, given the important role that a material's crystal structure has on defining and understanding its properties.

Here, we report the high-yield synthesis of colloidal SnS nanostructures that spans a range of distinct morphologies and sizes, including ∼12 nm cubes, ∼10 nm spherical polyhedra, and ∼270 nm square nanosheets. These particular systems are significant for several reasons. First, the SnS nanocubes represent a rare example of cube-shaped colloidal nanocrystals of a noncubic, layered material, and as such, these results provide important new insights into morphology control in the SnS system. Second, the morphological diversity facilitates systematic studies that ultimately establish important nanostructure−property correlations, which have not yet been reported for the SnS system. In particular, we show that the 0D SnS nanocubes and spherical nanopolyhedra are significantly more active for the photocatalytic degradation of methylene blue than their 2D nanosheet analogues. Finally, the quality, crystallinity, and size/shape diversity of the colloidal SnS nanocrystals allow in-depth crystallographic characterization in order to study their structural polymorphism, in particular with respect to their crystallization in the stable GeS structure type vs as metastable polymorphs such as ZB. Specifically, we show that a significant structural distortion emerges in SnS nanocrystals, which transforms the orthorhombic GeS structure type into a pseudotetragonal phase that is distinct from ZB. Importantly, this single pseudotetragonal phase accounts for all of the observed peaks in diffraction patterns that have previously been claimed to consist of a mixture of GeS-type SnS and ZB-type SnS. As such, these results help to rationalize and account for the discrepancies that exist between theoretical predictions of SnS polymorph stability and experimental claims.

EXPERIMENTAL SECTION

Materials. Tin(IV) chloride (99%), tin(II) acetate, oleic acid (90% tech), hexamethyldisilazane (>99%), and methylene blue hydrate were purchased from Sigma-Aldrich. Thioacetamide (99%), sulfur (99.5%), and 1-octadecene (90% tech) were purchased from Alfa Aesar. Oleylamine (>50%) and tri-*n*-octylphosphine (>85%) were purchased from TCI America. Solvents, including toluene, hexanes, acetone, and ethanol, were of analytical grade. All chemicals were used as received.

Synthesis of SnS Spherical Polyhedra. All reactions were performed under an argon atmosphere using standard Schlenk techniques. SnS spherical polyhedra were synthesized using a procedure modified from a literature report.[20] 1-Octadecene (5 mL, 15.6 mmol), oleic acid (4.5 mL, 14.2 mmol), and tri-*n*-octylphosphine (TOP) (3 mL, 6.7 mmol) were added to a 100 mL three-neck flask equipped with a condenser, thermometer, and septum and containing a magnetic stir bar. The reaction flask was sealed and placed in a heating mantle (Glass-Col) on a stir plate. To this was added 0.25 mL (2.1 mmol) of tin(IV) chloride ($SnCl_4$) through the septum using a syringe. While being stirred vigorously, the reaction flask was evacuated and raised to 120 °C for 10 min to remove any residual water. After lowering the temperature to 90 °C, the reaction solution was put under an argon blanket and 1 mL (4.8 mmol) of hexamethyldisilazane (HMDS, bis[trimethylsilyl]amine) was added through the septum with a syringe, causing the solution to turn from clear to milky white in color. The temperature was raised to 140 °C, and a 0.077 M thioacetamide solution consisting of 0.075 g (1.0 mmol) thioacetamide dissolved in 10 mL (30.4 mmol) of oleylamine and 3 mL (6.7 mmol) of TOP was injected all at once. The solution rapidly turned dark brown, and the temperature briefly dropped to ∼125 °C before quickly recovering. The temperature was maintained at 140 °C for 1 h before removing the reaction flask from the heating mantle and allowing it to cool to room temperature.

Synthesis of SnS Cubes. SnS cubes were synthesized similarly to SnS spherical polyhedra, with some modifications. After adding HMDS at 90 °C, the temperature was raised to 170 °C. A larger-volume 0.077 M thioacetamide solution was prepared, consisting of 0.15 g (2.0 mmol) of thioacetamide dissolved in 20 mL (60.8 mmol) of oleylamine and 6 mL (13.4 mmol) of TOP. Five milliliters of this thioacetamide solution was injected all at once, causing the color to turn from milky white to black and the reaction temperature to drop from 170 to ∼155 °C before recovering quickly. The remaining 21 mL of growth solution was then added dropwise with a syringe through the septum, taking care to maintain the reaction temperature at 165−170 °C. After the last of the growth solution was added, the reaction was allowed to proceed at 165−170 °C for 5 min before removing the flask from the heating mantle and allowing it to cool to room temperature. For aliquot studies, a portion of the reaction was removed with a syringe through the septum. SnS nanocrystal samples were collected from solution by adding ethanol in a 1:1.5 solvent:cosolvent ratio and centrifuging at 12 000 rpm for 3 min. After decanting the supernatant, the dark brown precipitate was redispersed in toluene. This solution was then centrifuged at 6000 rpm for 1 min, with the supernatant collected and precipitate discarded.

Synthesis of SnS Sheets. To synthesize SnS nanosheets, 24 mg (0.10 mmol) of tin(II) acetate ($Sn[OAc]_2$) was dissolved by sonication in 20 mL (60.8 mmol) of oleylamine and added to a 100

dx.doi.org/10.1021/ja405203e | J. Am. Chem. Soc. 2013, 135, 11634−11644

mL three-neck flask equipped with a condenser, thermometer, and septum and containing a magnetic stir bar. Then 110 μL of a 1 M solution of oleylamine–sulfur [320 mg (10 mmol) of sulfur in 10 mL (30.4 mmol) of oleylamine, resulting in a dark red solution] was also added. The reaction flask was sealed and placed in a heating mantle on a stir plate. While being stirred vigorously, the reaction flask was evacuated and raised to 120 °C for 10 min to remove any residual water. After the temperature was lowered to 90 °C, the reaction solution was put under an argon blanket and 1 mL of HMDS was added through the septum with a syringe. The temperature was then raised to 180 °C at about 10 °C/min, resulting in a black solution. After an additional 30 min at 180 °C, the flask was removed from the heating mantle and allowed to cool to room temperature. The reaction solution was added to 30 mL of a 3:1:1 acetone:hexanes:toluene mixture and centrifuged at 12 000 rpm for 10 min to yield a black precipitate. After decanting the supernatant, the SnS nanosheets were redispersed in toluene. Next, an equal volume of ethanol was added as a cosolvent, and this solution was centrifuged again at 12 000 rpm for 10 min. The precipitate was collected and redispersed in toluene for storage.

Photocatalytic Degradation of Methylene Blue. Solutions of SnS dispersed in toluene were precipitated by adding ethanol in a 1:1.5 ratio and centrifuging at 12 000 rpm for 3 min. After decanting the supernatant, the dark brown precipitate was dried under vacuum overnight. Two milligrams of the resulting powder was then weighed out and dissolved in 1 mL of toluene using a sonic bath. This solution was then pipeted into a quartz cell containing a stir bar and 2 mL of a 0.008 mg/mL aqueous solution of methylene blue hydrate. The cell was placed on a stir plate under a 300 W Xe lamp AM1.5G solar simulator (Newport, output power adjusted to 100 mW/cm^2) and mixed in the dark for 5 min to equilibrate. Next, an initial ultraviolet–visible (UV–vis) absorption spectrum of the aqueous phase was collected, using a fiber optic spectrometer (Ocean Optics), by removing the cell from the stir plate and allowing the immiscible solvents to quickly separate. The cell was then placed back on the stir plate and the shutter was opened, exposing the solution to visible light by using a UV cutoff filter (λ > 420 nm) and IR water filter. At 2.5-min intervals, the shutter was closed and a UV–vis absorption spectrum was collected of the aqueous layer until the degradation of the methylene blue was completed, as judged by the relative absorption at 663 nm compared to the baseline.

Characterization. Transmission electron microscopy (TEM) images were obtained from a JEOL 1200 EX II microscope operating at 80 kV. Particle size distribution was determined with ImageJ software (http://rsbweb.nih.gov/ij/) using a minimum of 200 individual particles. SnS nanocube diameter was taken as the edge length. High-resolution TEM (HRTEM) images, selected area electron diffraction (SAED) patterns, and nanobeam diffraction (NBD) patterns were collected using a JEOL 2010 LaB_6 microscope and a JEOL 2010F field emission microscope, both operating at an accelerating voltage of 200 kV. Scanning transmission electron microscopy coupled with energy-dispersive X-ray spectroscopy (STEM-EDS) were performed using the JEOL 2010F, which is outfitted with an EDAX solid-state X-ray detector. ES Vision software (Emispec) was used for EDS data processing, with the Sn L-shell and S K-shell transitions, which do not appreciably overlap, chosen for quantitative EDS analysis. All microscopy samples were prepared by casting one drop of dispersed SnS in toluene onto a 400 mesh Formvar and carbon-coated copper grid (Electron Microscopy Sciences). Lattice spacings and crystallographic structure were determined from the fast Fourier transform (FFT) of the HRTEM images, using Gatan Digital Micrograph software. Powder X-ray diffraction (XRD) patterns were collected with samples drop-cast on an amorphous plate using a Bruker Advance D8 X-ray diffractometer and Cu Kα radiation at room temperature. Simulated atomic structures, powder XRD patterns, and electron diffraction patterns were made using the CrystalMaker software suite. 3D crystal structures were modeled using WinXMorph.[31] UV–vis absorption data were measured on SnS/toluene solutions in a quartz cuvette using an Ocean Optics HR4000 spectrometer with a DH-2000-BAL light source. Ultraviolet–visible–near-infrared (UV–vis–NIR) diffuse reflectance measurements were obtained using a Perkin-Elmer Lambda 950 spectrophotometer equipped with a 150 mm integrating sphere. UV–vis–NIR samples were prepared by drop-casting a concentrated solution of SnS dispersed in toluene onto a quartz substrate.

RESULTS AND DISCUSSION

Synthesis of SnS Nanocubes, Spherical Nanopolyhedra, and Nanosheets. Figure 1 shows representative TEM images of the as-synthesized SnS cubes and spherical polyhedra at two different magnifications. The nanocrystals are largely uniform in both size and morphology. Statistical analysis of the SnS nanocubes revealed an average edge length of 11.5 ± 1.9 nm and an estimated morphological yield of 95%. For the SnS spherical polyhedra, the average diameter was 9.7 ± 1.5 nm, with an estimated morphological yield of 92%. The remaining ~8% of the sample consisted of particles that were roughly tetrahedral or pyramidal in morphology and collectively are similar in shape to previously reported SnS particles.[19,20] SAED patterns for an ensemble of particles (Figure 1b,e) indicate that both morphologies are highly crystalline and of the same crystal structure. However, the cubes display noticeable preferred orientation (evidenced by some differences in the relative intensities of the diffraction rings) because they were drop-cast onto the sample grid and therefore align preferentially with the faces of the cubes exposed. No oxide shell was visible, and wide-area EDS analysis, along with STEM-EDS linescans across individual particles (Supporting Information, Figure S1), indicated a nearly 1:1 atomic ratio of Sn to S (52% Sn, 48% S), confirming the SnS stoichiometry.

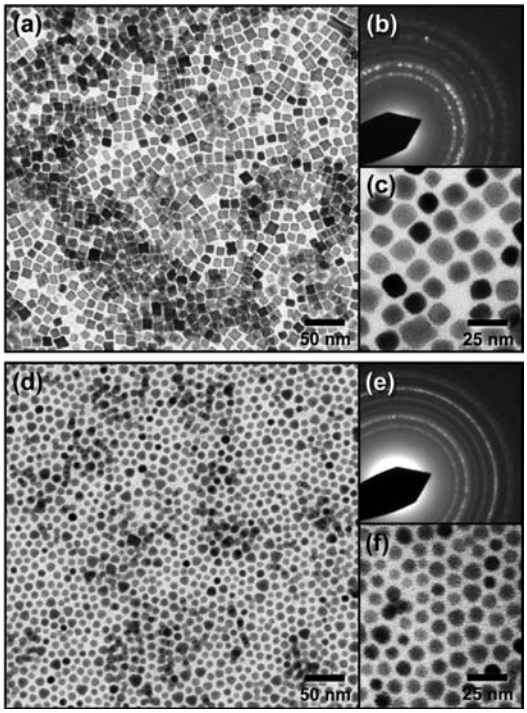

Figure 1. Representative TEM images (two magnifications) and SAED patterns of SnS cubes and spherical polyhedra: (a, c) ~12 nm SnS cubes with (b) corresponding SAED pattern and (d, f) ~10 nm spherical polyhedra with (e) corresponding SAED pattern.

To compare the zero-dimensional (0D) SnS nanocrystals described above to larger two-dimensional (2D) nanostructures in the sections that follow, SnS sheets were also synthesized.

dx.doi.org/10.1021/ja405203e | J. Am. Chem. Soc. 2013, 135, 11634–11644

Representative TEM images of the SnS sheets are shown in Figure 2. The sample consists of ~2/3 square nanosheets, with

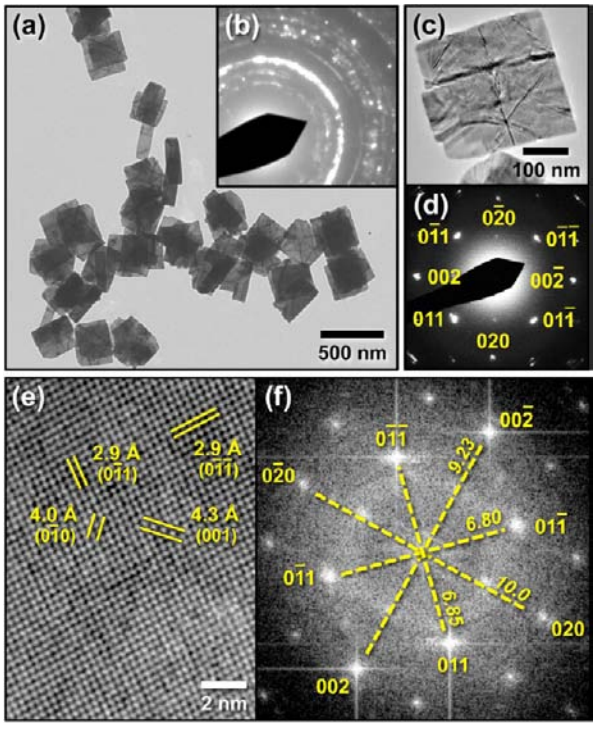

Figure 2. (a) Representative TEM image of a group of SnS nanosheets with (b) the corresponding SAED pattern and (c) TEM image of a single SnS nanosheet with (d) the corresponding SAED pattern, which can be indexed to SnS(100). (e) HRTEM image of a single SnS nanosheet and (f) the resulting FFT. The lattice fringe measurements in part e, as well as the arrangement and reciprocal space distances of diffraction spots in part f, can be indexed to the (100) surface of α-SnS, corroborating the SAED patterns. All reciprocal distances in part f are in units of nm^{-1}.

an average edge length of 270 ± 50 nm, and ~1/3 higher aspect ratio rectangular nanosheets. Importantly, only 2D nanosheets were observed in this sample, indicating a nearly quantitative 2D morphological yield. Monodisperse 1D nanobelts and 2D nanosheets have been reported previously for SnS,[11,29,32−34] as well as for other GeS-type semiconductors including GeS, GeSe, and SnSe.[35,36] However, to our knowledge, this represents the first report of laterally uniform, square-shaped 2D nanosheets of SnS with all edge lengths <500 nm, in contrast to previous reports with edge lengths >1 μm. The polycrystalline SAED pattern shown in Figure 2b corresponds to an ensemble of nanosheets and is consistent with GeS-type SnS. Analysis of an individual sheet (Figure 2c) by SAED (Figure 2d) indicates that it is single-crystalline and can be indexed to the (100) plane of α-SnS, which adopts the orthorhombic GeS structure type that is nominally the most stable SnS polymorph. The starburst fringes seen on the surface of the SnS sheet in Figure 2c are likely due to buckling and have been observed for other thin 1-D and 2-D nanostructures.[11,29,32−34] HRTEM imaging of the sheets (Figure 2e) confirms their single-crystalline nature, and the corresponding FFT (Figure 2f) corroborates the diffraction pattern in Figure 2d. Measurements of the reciprocal space distances between the FFT diffraction spots were quantitatively consistent with those of the SAED pattern, their inverse values matched well with the lattice fringes of the HRTEM image, and they were indexed to the (100) plane of α-SnS (Supporting Information, Figure S2 and Table S1). Although some measurement error is unavoidable due to slight deviation from the zone axis (for example, the two {011} d-spacings calculated in Table S1 of the Supporting Information vary by 0.02 Å), it can be mitigated through analysis of an ensemble of nanostructures. From these measurements, the interatomic distances for the (010) and (001) planes were determined to be 3.98 and 4.34 Å, respectively. These correspond to the b and c lattice constants of orthorhombic GeS-type SnS, respectively, and their values match those of bulk SnS (b = 3.98 Å, c = 4.33 Å).[37] This explicitly establishes that quantitative FFT analyses of high-quality HRTEM images can be used to extract accurate interatomic distances and lattice constants, analogous to electron diffraction data.

Powder X-ray Diffraction Patterns of SnS Nanostructures. Figure 3 shows the powder XRD pattern for a

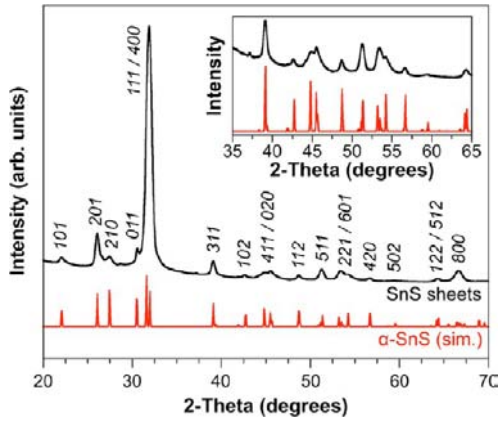

Figure 3. Powder XRD pattern of SnS nanosheets (black), which matches the simulated pattern of α-SnS (red). The relatively high intensity of the (400) and (800) reflections indicates a preferred orientation in the [100] direction. Inset: an expanded region between 35° and 65° 2θ, highlighting the good agreement between the experimental and simulated patterns.

representative drop-cast solution of SnS nanosheets. The pattern matches well with the simulated pattern for α-SnS. As is commonly observed for other GeS-type 1D and 2D nanostructures, the drop-cast SnS sheets showed high relative intensities for the (400) and (800) Bragg reflections. This indicates preferred orientation in the [100] direction, which is orthogonal to the layers that bulk α-SnS inherently tends to form. The lattice constants of the sheets were determined from the powder XRD data to be a = 11.18 Å, b = 3.98 Å, and c = 4.32 Å, which agree with the literature values for α-SnS (a = 11.18 Å, b = 3.98 Å, c = 4.33 Å)[37] and are also consistent with the SAED and HRTEM FFT analyses of the (100) plane, as discussed in the previous paragraph (Figure 2 and Supporting Information, Table S1). Importantly, this establishes that the interatomic distances as determined from quantitative FFT analyses of high-quality HRTEM images for a known crystallographic plane can also be reasonably correlated to powder XRD data.

Figure 4 shows the powder XRD patterns for drop-cast solutions of the SnS cubes and spherical polyhedra from Figure 1. Scherrer analysis of the most intense reflections yielded a calculated crystallite size of 13 nm for the SnS cubes and 11 nm

dx.doi.org/10.1021/ja405203e | J. Am. Chem. Soc. 2013, 135, 11634−11644

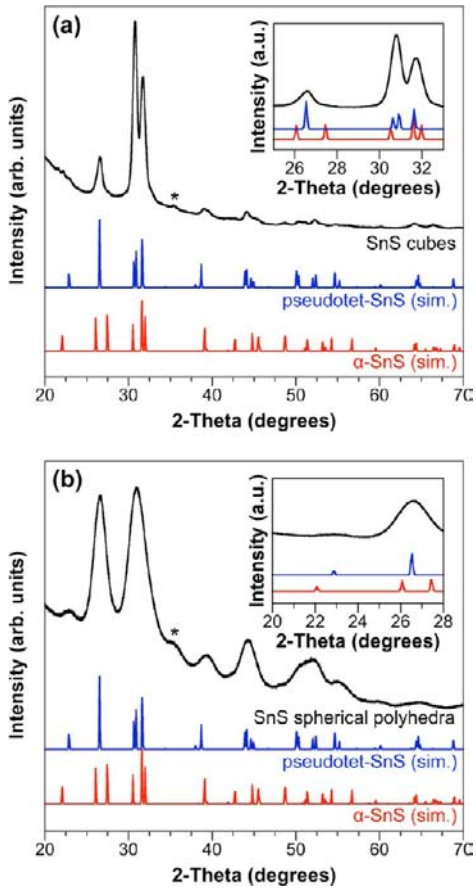

Figure 4. Powder XRD patterns (black) of (a) SnS cubes and (b) SnS spherical polyhedra showing simulated patterns for α-SnS (red) and the proposed pseudotetragonal modification of SnS (blue). The insets show expanded characteristic regions that highlight the significantly better agreement with the powder XRD patterns of pseudotetragonal-SnS than with α-SnS. The asterisk (*) indicates an SnO_2 impurity.

for the spherical polyhedra, which is in good agreement with the average particle sizes determined by TEM. This suggests that the cubes and spherical polyhedra are largely single-crystalline. Compared to the powder XRD pattern of the SnS sheets in Figure 3, the powder XRD patterns of the 0D nanocrystals in Figure 4 appear noticeably different, and they do not match as well with the simulated diffraction pattern of α-SnS (red patterns in Figure 4). Most apparent is that the reflections corresponding to the (201) and (210) planes, which are separate and distinct for α-SnS at 26.0° and 27.5° 2θ, respectively (Figure 3), have been replaced by a single reflection at 26.5° 2θ (Figure 4a,b). Additionally, the most intense reflections of both the SnS cubes and spherical polyhedra (located at 30.8° and 31.0° 2θ, respectively) do not precisely correspond to any reflection in the pattern of α-SnS. Other more subtle, but significant, differences in the XRD patterns for the SnS cubes and spherical polyhedra vs the SnS sheets include shifts in the positions of the (101) reflection from 22.0° to 22.9° 2θ, the (411) reflection from 44.8° to 44.1° 2θ, and the (601) reflection from 53.4° to 52.4° 2θ. The reflection at 35° 2θ corresponds to a small amount of SnO_2. The differences in relative intensities between the reflections in Figure 4a vs those in Figure 4b are due to preferred orientation in the nanocubes samples, which does not occur for the spherical polyhedra.

The powder XRD patterns for the 0D nanocrystals are clearly distinct from those of the sheets. Indeed, the powder XRD patterns in Figure 4, for the cubes and spherical polyhedra are consistent with those previously reported to correspond to mixtures of metastable ZB-type SnS and GeS-type α-SnS.[11,19,21,25−29] However, by adjusting the lattice constants to a = 11.55 Å, b = 4.12 Å, c = 4.12 Å (distinct from the lattice constants of α-SnS, which are a = 11.18 Å, b = 3.98 Å, c = 4.33 Å)[37] while all other crystallographic parameters are kept the same, we were able to generate a single-phase simulated diffraction pattern that matched well with the experimental powder XRD patterns for the SnS cubes and spherical polyhedra (Figure 4, blue pattern). We arrived at these lattice constants, in part, by recognizing that the (201) and (210) reflections largely overlap, which suggests that the b and c lattice constants are equal or nearly so. Therefore, the SnS crystal structure that corresponds to the experimentally observed powder XRD patterns for the cubes and spherical polyhedra is best described as pseudotetragonal. Such crystallographic distortions are not unprecedented, as 0D nanocrystals of SnSe, which is isostructural with SnS in the bulk form, were reported to distort from a *Pnma* space group to *Cmcm* with decreasing particle size.[38]

A direct comparison of the simulated diffraction patterns of α-SnS and of the modified pseudotetragonal form can be seen in Figures 5 and S3 (Supporting Information). In addition to

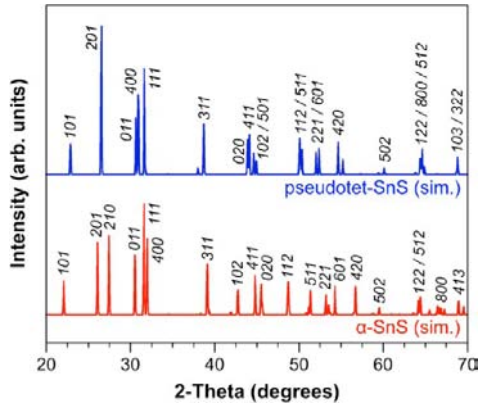

Figure 5. Direct comparison of the simulated powder XRD patterns of orthorhombic α-SnS and the proposed pseudotetragonal modification of SnS, highlighting the numerous reflections that are shifted.

the aforementioned shift in the (201) and (210) reflections, relatively intense reflections in the simulated XRD pattern for the pseudotetragonal form [(011) at 30.7° 2θ and (400) at 30.9° 2θ] now fall directly at the Bragg angle of the highest-intensity reflections in the experimental XRD patterns for the SnS cubes and spherical polyhedra. Additionally, the observed (101), (411), and (611) reflections match well with those expected on the basis of the simulated XRD pattern. However, in order to further compare the crystal structure associated with the SnS cubes and spherical polyhedra to the experimental and simulated powder XRD patterns, especially to verify that the collection of experimentally observed reflections are attributable to a single-phase pseudotetragonal form of SnS and not due to a mixture of phases, HRTEM with FFT analyses were performed, as was done for the SnS sheets. Note again that HRTEM analysis of single particle surfaces has been established as a reasonable means of measuring interatomic distances of

dx.doi.org/10.1021/ja405203e | J. Am. Chem. Soc. 2013, 135, 11634−11644

indexed planes,[39−41] which can subsequently be used to corroborate powder XRD data.

Crystallographic Analysis of Cubes and Spherical Polyhedra Using HRTEM Images. Figure 6b−d shows HRTEM images of two representative single-crystal SnS cubes and their corresponding FFTs. The FFTs of both images were indexed to the (011) plane of bulk SnS on the basis of the pattern of the diffraction spots, and the electron beam was oriented very close to the [011] zone axis. These FFT patterns were corroborated by single-particle nanobeam diffraction (Supporting Information, Figure S4). Furthermore, the arrangement of 2D lattice fringes on the surface of the particle is visible in Figure 6b, which corresponds to the distinctive two up, two down pattern of atoms proceeding in the [100] direction of the (011) surface, as seen in simulated models of that atomic plane (Figure 6a). However, despite the qualitative correlation between the FFT and the expected diffraction pattern of α-SnS, quantitative measurements differed. The reciprocal space distances from spots in the diffraction pattern to their inverses, going through the central spot, can be converted to interatomic distances on that crystalline facet, and these values did not correspond with those expected on the basis of the simulated diffraction pattern of α-SnS. As seen by comparison of parts d and e of Figure 6, the reciprocal distance between the {400} diffraction spots was found to be 6.94 nm^{-1} instead of 7.16 nm^{-1}, which is the value that would be expected for α-SnS. Likewise, the distance between the {011} spots was 6.88 nm^{-1} instead of 6.80 nm^{-1}, the distance between the {111} spots was 7.08 nm^{-1} instead of 7.03 nm^{-1}, and the distance between the {411} spots was 9.76 nm^{-1} instead of 9.87 nm^{-1}. While these distances did not match those of α-SnS, they did match well with the simulated diffraction pattern of the distorted pseudotetragonal form of SnS (Figure 6f), which was generated using lattice constants determined from analysis of the powder XRD data. Direct measurement of the lattice fringes visible by HRTEM provides substantially less resolution of interatomic distances than the complementary FFT. However, Figure 6b,c displays measured distances of 2.9 Å for both the {400} and {011} lattice fringes, and these corresponded well with the values determined from the FFT analysis, after conversion from reciprocal space to real space. HRTEM analysis of 30 randomly chosen cubes indicated that 22 were oriented such that their top facet could be indexed, via FFT analysis, to one of the four {011} planes of pseudotetragonal SnS. This strongly suggests that four of the six primary facets of the SnS cubes are bound by planes of the form {011}. Similarly, HRTEM analysis of the spherical polyhedra revealed that they too were single-crystalline and many were bound by similar {011} facets (Supporting Information, Figure S5), although a smaller fraction (13 out of 30).

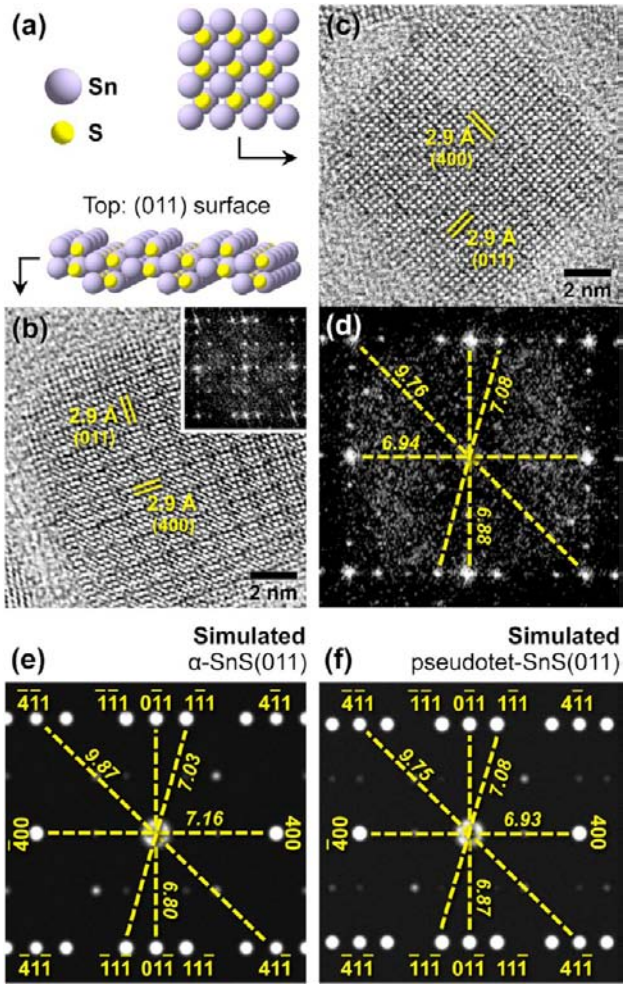

Figure 6. (a) Atomistic models of the SnS(011) surface of the proposed pseudotetragonal modification of SnS. (b) HRTEM image of a SnS nanocube taken slightly offset from the [011] zone axis (inset: resulting FFT) to display fringes corresponding to the same atomic arrangement seen in part a. (c) HRTEM image of a SnS nanocube taken from the [011] zone axis with measured lattice fringes and (d) the resulting FFT, which can be indexed to SnS(011). Quantitative analysis of the reciprocal distances between inverse diffraction spots seen in part d do not correspond well with the simulated electron diffraction pattern of α-SnS(011) in part e but are an excellent match with the simulated electron diffraction pattern of pseudotetragonal SnS(011) in part f. FFTs in parts b and d have been rotated for ease of comparison. All reciprocal distances are in units of nm^{-1}.

Further HRTEM/FFT characterization indicated that the SnS cubes (Supporting Information, Figures S6 and S7) and spherical polyhedra (Figure 7a) were also bound by a second, different crystallographic plane. The arrangement of diffraction spots (Figure 7b) suggested that this facet belongs to the {h11} family of planes (Supporting Information, Figure S8a). Quantitative FFT analysis suggested that this facet must be a higher index plane of the form {h11}, although we cannot unambiguously attribute the pattern to a specific hkl plane because the difference in spacings between diffraction spots for high-index h11 planes is extremely small. However, the values obtained, as detailed below, are measurably different than most obvious low-index possibilities, including (111), which argues strongly for the presence of a high-index facet, which we tentatively label as (15 1 1) on the basis of the measured reciprocal distances between inverse diffraction spots (Figure 7c,d). The angle at which (15 1 1) slices through the unit cell approaches that of (100), thus giving rise to a similar diffraction pattern (Supporting Information, Figure S8b), but with measurably different spacings. Note that additional diffraction spots are visible in all of our FFTs compared to the simulated patterns, and these likely emerge from the periodic contrast differences that appear during HRTEM imaging. The reciprocal distances measured on the FFT (Figure 6b) were 6.90 nm^{-1} between the {011} diffraction spots, 7.04 nm^{-1} between the {111} spots, 9.70 nm^{-1} between the {020} spots, and 9.90 nm^{-1} between the {102} spots. All of these correspond well with the simulated high-index {h11} pattern for pseudote-

dx.doi.org/10.1021/ja405203e | J. Am. Chem. Soc. 2013, 135, 11634−11644

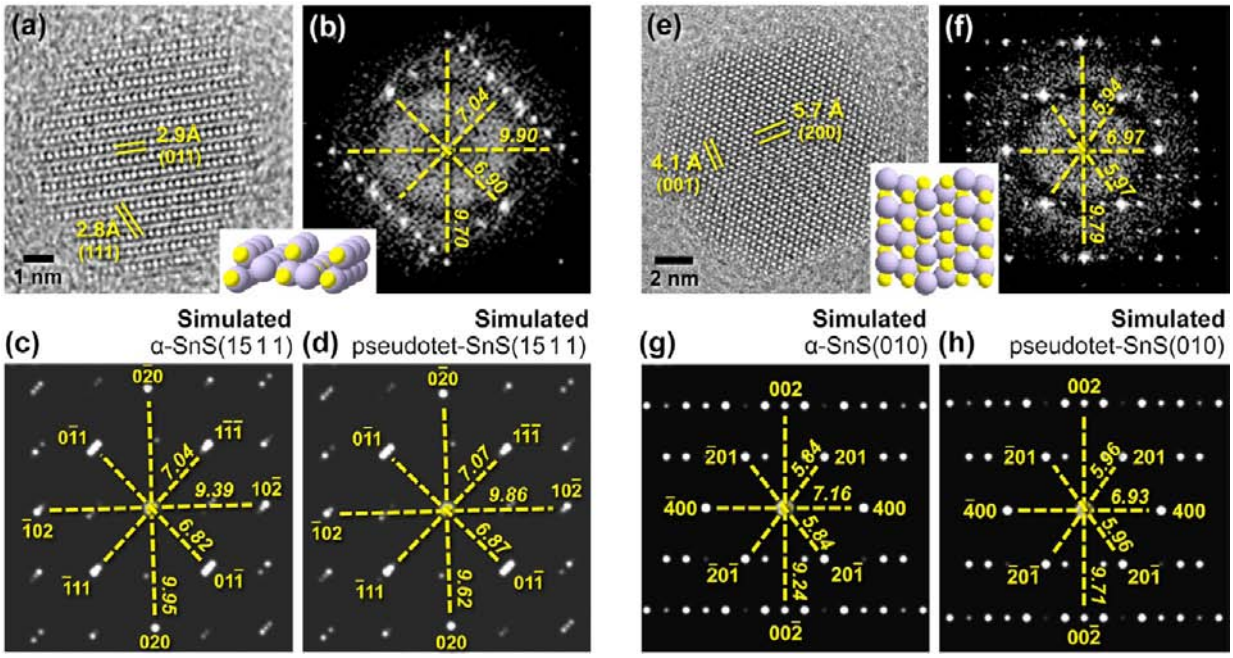

Figure 7. (a) HRTEM image of a SnS spherical polyhedron with measured lattice fringes and (b) the resulting FFT, which can be indexed to a high-index SnS(h11) plane. The inset shows the atomistic model of pseudotetragonal SnS(h11). Quantitative analysis of reciprocal distances between inverse diffraction spots seen in part b correspond well with the simulated electron diffraction pattern of pseudotetragonal SnS(15 1 1) in part c, but do not match well with that of α-SnS(15 1 1) (d) or any other α-SnS plane. (e) HRTEM image of a SnS spherical polyhedron taken from the [010] zone axis with measured lattice fringes and (f) the resulting FFT, which can be indexed to SnS(010). The inset shows the atomistic model of pseudotetragonal SnS(010). Similar quantitative analysis of part f revealed reciprocal distances that could not be reconciled with the simulated diffraction pattern of α-SnS(010) in part g but that matched well with the simulated diffraction pattern of pseudotetragonal SnS(010) in part h. FFTs in parts b and f have been rotated for ease of comparison. All reciprocal distances are in units of nm^{-1}.

tragonal SnS but cannot be quantitatively reconciled with a high-index (h11) plane of α-SnS. The HRTEM image (Figure 7a) also matches well with an (h11) plane of pseudotetragonal SnS, which is simulated in the inset between parts a and b of Figure 7. Measurement of the atomic spacings resulted in distances of 2.9 and 2.8 Å, which are indexed to the {011} and {111} planes, respectively.

A third primary facet that was observed by HRTEM for the SnS spherical polyhedra, but not for the cubes, can be seen in Figure 7e. The resulting FFT of this image reveals a diffraction pattern that can be indexed to SnS(010) for α-SnS (Figure 7f). However, once again, measurement of the reciprocal distance between the diffraction spots and their inverses does not quantitatively match the values for α-SnS, simulated in Figure 7g. The reciprocal distance between the {400} spots is 6.97 nm^{-1}, between the {002} spots is 9.79 nm^{-1}, and between the sets of {201} spots is 5.97 and 5.94 nm^{-1}, all of which are very close to the values found in the simulated electron diffraction pattern of the (010) plane for the pseudotetragonal form (Figure 7h). The HRTEM image reveals lattice fringes of 5.7, 4.1, and 3.3 Å. These values correspond to the {200}, {001}, and {201} planes of pseudotetragonal SnS, respectively, and are in agreement with the simulated (010) crystal face.

Collectively, these comparisons between the HRTEM FFTs of individual nanocrystal facets and the simulated electron diffraction patterns of α-SnS indicate that there is a distortion in the crystal structure of the SnS cubes and spherical polyhedra that was not observed in the nanosheets. Furthermore, this distortion is consistent with the shifted reflections that were observed in the corresponding powder XRD patterns. HRTEM FFT analysis of a series of nanocrystals (Supporting Information, Figure S9) indicates that, although there is some particle-to-particle variation in reciprocal distances due to slight deviation from the zone axis orthogonal to the face of each particle, the measured values are all self-consistent. By analyzing an ensemble of nanocrystals and calculating the average values, we determined that the mean distances between the {400} diffraction spots is 6.91 nm^{-1}, between {020} (and also {002}) is 9.67 nm^{-1}, between {011} is 6.84 nm^{-1}, between {201} (and also {210}) is 5.94 nm^{-1}, between {111} is 7.07 nm^{-1}, and between {411} is 9.75 nm^{-1}. These reciprocal space measurements correspond to real space distances of 2.89 Å for (400), 2.07 Å for (020)/(002), 2.92 Å for (011), 3.37 Å for (201)/(210), 2.83 Å for (111), and 2.05 Å for (411), respectively (Supporting Information, Table S2). The lattice constants can be extracted directly from the lattice spacings of the (400) and (020)/(002) planes as a = 11.56 Å and b = c = 4.14 Å, which nearly precisely corroborates the values of the pseudotetragonal modification that was determined by analysis of the powder XRD data. Additionally, the corresponding mean d-spacing of (201)/(210) is equivalent to 26.5° 2θ, of (011) is equivalent to 30.6° 2θ, of (400) is equivalent to 31.0° 2θ, and of (411) is equivalent to 44.2° 2θ. All of these values closely match the Bragg reflections of our experimental powder XRD patterns, as well as the powder XRD pattern that was simulated on the basis of the pseudotetragonal modification. However, these values cannot be reconciled with the reflections associated with α-SnS. This verifies that the HRTEM FFT data of the nanocrystals is consistent with the powder XRD data, and furthermore, that a structural distortion from orthorhombic GeS-type α-SnS to a pseudotetragonal modification has occurred in the cubes and spherical polyhedra. Importantly, the HRTEM data are not

dx.doi.org/10.1021/ja405203e | J. Am. Chem. Soc. 2013, 135, 11634−11644

consistent with, and show no evidence of, a mixture of GeS-type and ZB-type SnS.

Six polymorphs of SnS have been reported in the literature. Most common and most stable in bulk systems is orthorhombic α-SnS,[42] which favors the formation of two-dimensional structures such as the SnS nanosheets because of its nominally layered structure. At high temperatures, it has been reported that α-SnS undergoes a gradual phase transition to the TlI-type β-phase.[43] Eventually the unit cell becomes pseudotetragonal, with lattice constants that are very similar to those measured for our SnS cubes and spherical polyhedra (a = 11.48 Å, b = 4.18 Å, c = 4.15 Å). However, this lattice distortion is accompanied by a significant alteration of atomic positions and a change in space group from *Pnma* to *Cmcm*. Accordingly, the electron diffraction patterns predicted for β-SnS do not match those observed for our SnS cubes and spherical polyhedra (Supporting Information, Figure S10). γ-SnS is a monoclinic distortion that forms at high pressures, and it does not match with our experimental observations.[44] The recently discovered δ-SnS polymorph is an orthorhombic distortion of the GeS-type structure that was also a poor match for our nanocrystal diffraction patterns. However, as with β-SnS, there was a substantial expansion of the crystal lattice in the a-direction relative to that of α-SnS.[45] The other polymorphs of SnS are a NaCl-type phase, which has been reported very rarely,[46,47] and a ZB-type phase (Supporting Information, Figure S11).[48] However, the substantial asymmetry seen in our nanocrystal FFTs precludes either of these cubic structures. Collectively, the XRD patterns and HRTEM FFTs of our SnS nanocrystals cannot be indexed fully to any of these established polymorphs. While we cannot unambiguously determine a space group and explicitly solve the crystal structure using the available data, our experimental observations match best with the pseudotetragonally distorted modification of α-SnS discussed earlier. With this distortion, the unit cell is stretched in the a direction such that both the layer thickness and the gaps between layers increases, while Sn and S become more equidistant to their four nearest in-plane neighbors due to the essentially equivalent dimensions of the unit cell in the b and c directions.

This distorted modification of α-SnS is important, because it helps to rationalize the diffraction patterns that are increasingly observed for nanoparticles and films of SnS. Inspection of a number of published SnS diffraction patterns reveals that there are many reported nanostructures with powder XRD patterns that are highly similar to those shown for the cubes and spherical polyhedra in Figure 4 and therefore could also potentially be indexed to this pseudotetragonal modification of α-SnS.[11,19,21−23,25−29,49,50] Notably, it is frequently hypothesized that these diffraction patterns correspond to a mixture of metastable ZB-type SnS and GeS-type α-SnS. While such a mixture indeed can yield diffraction patterns similar to those shown in Figure 4 (Supporting Information, Figure S12), extensive HRTEM/FFT analysis of the SnS cubes and spherical polyhedra yielded no evidence of a cubic ZnS polymorph. Indeed, the experimental observation of metastable ZB-type SnS has been called into question by a recent report, which claimed that first principles calculations suggest that ZB-type SnS is thermodynamically unfavorable and has been misidentified in the literature.[30] Therefore, we suggest that some of these SnS powder diffraction patterns may be misassigned as mixtures and instead can be accounted for by a single phase: a pseudotetragonal modification of α-SnS, which merges the results from XRD, HRTEM/FFT, and electron diffraction.

Further support for this hypothesis is provided by HRTEM analysis of the pyramid-shaped impurities in our samples of spherical polyhedra, which reveals that they are bound primarily by facets that can be indexed to the {210} and {201} planes of pseudotetragonal SnS (Supporting Information, Figure S13). These pyramids are very similar morphologically to the nanostructures seen in some previous reports of ZB-type SnS,[19,21,22] and the electron diffraction pattern of a crystal of pseudotetragonal SnS(210)/(201) appears similar to that of a cubic (111) facet. Notably, although it is well-known that the kinetic barrier to structural transitions decreases substantially with nanocrystal size,[51] the structures exhibiting powder XRD patterns that can potentially be indexed to a pseudotetragonal phase of SnS are not limited to a small size regime. Diffraction patterns from larger 3D SnS structures and coarse thin films reported in the literature appear similar to those of the 0D nanocrystals,[19,21,27,28] while 1D belts and 2D sheets have exclusively been reported as α-SnS. Interestingly, there are reports that 3D SnS nanostructures with diffraction patterns similar to those of our nanocrystals (e.g., pseudotetragonally modified α-SnS) convert to 1D belts (with flat surfaces) of the standard α-SnS structure.[11,29] This suggests that the pseudotetragonal distortion may occur only (or preferentially) in nanostructures that are not flat.

Formation Pathway and 3D Model of SnS Nanocrystals. The in-depth analysis of the exposed crystal planes discussed above, coupled with careful control studies, provide insights into how the SnS cubes and spherical polyhedra form. Gradual addition of thioacetamide is necessary to generate cubes in high yield, whereas spherical polyhedra reactions call for a rapid addition, suggesting that slower growth kinetics is required for SnS nanocube formation. However, reaction temperature is also an important formation parameter, as thermodynamics, in addition to kinetics, can influence morphological yields of nanocrystals.[52] We observe that lower-temperature nanocube reactions (e.g., 140 °C instead of 170 °C) produce a larger population of spherical polyhedra, while higher temperature spherical polyhedra reactions (e.g., 170 °C instead of 140 °C) produce a larger population of nanocubes (Supporting Information, Figure S14). At 240 °C, the particles are agglomerated and morphologically ill-defined. This indicates that spherical polyhedra are favored at lower temperatures, while cubes are favored at intermediate temperatures, and high temperatures are unsuitable.

TEM images of aliquots taken during the synthesis of SnS cubes and spherical polyhedra provide additional insights into how they form. For the spherical polyhedra (Supporting Information, Figure S15), ∼5 nm crystals have already formed 1 min after injection at 140 °C, and they grow to ∼8 and ∼10 nm after 5 min and 1 h, respectively. For the cubes, an aliquot collected after the initial injection but prior to the gradual addition of thioacetamide consists almost entirely of spherical polyhedra (Figure 8a−c). Subsequent gradual addition of thioacetamide over 5 min causes the facets of the spherical polyhedral seeds to fill in, transforming them into cubes and accordingly increasing their size to the final ∼12 nm diameter (Supporting Information, Figure S16). These results suggest that the SnS cubes form through spherical seed-mediated overgrowth, which is a pathway that is well-known to produce a diverse library of nonthermodynamic nanocrystal shapes.[53,54] It also suggests that the molecular species present during synthesis preferentially adsorb to the {011} and {h11} facets, thereby lowering their surface energy, as {010}/{001} facets are

dx.doi.org/10.1021/ja405203e | J. Am. Chem. Soc. 2013, 135, 11634−11644

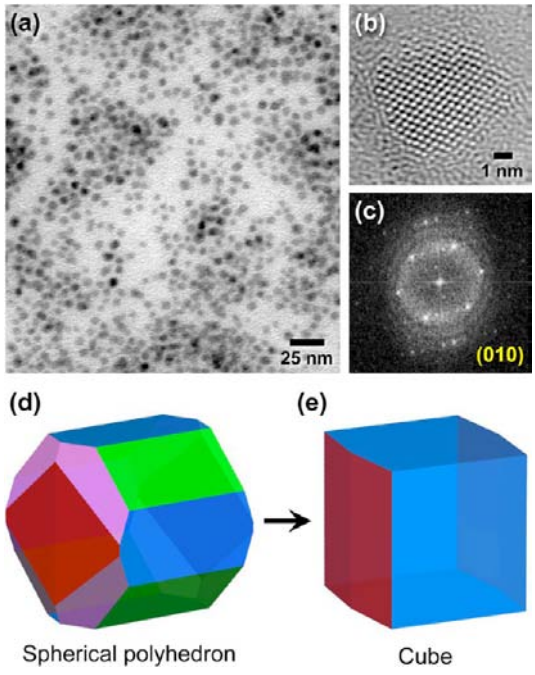

Figure 8. (a) TEM image of an aliquot taken during the formation of SnS cubes after initial injection of thioacetamide, but prior to subsequent gradual addition. (b) Representative HRTEM image, indicating that these nanocrystals were spherical polyhedra, confirmed by (c) the resulting FFT, which can be indexed to the (010) plane of pseudotetragonal SnS (not present in cubes). Idealized 3D models of (d) a SnS spherical polyhedron and (e) a SnS cube. On the basis of detailed crystallographic analysis, the spherical polyhedron is hypothesized to be bound by facets of {011} [blue], {h11} ($h \approx 15$) [red], {010}/{001} [green], and {210}/{201} [purple]. Overgrowth occurs in the ⟨010⟩/⟨001⟩ and ⟨210⟩/⟨201⟩ directions to form the cubes, which are bound by {011} and {h11} facets.

only present when the nanocrystals are small and energetics are dominated by a minimization of surface area.[55]

On the basis of the HRTEM analysis of exposed nanocrystal facets described previously, the direction of spherical seed overgrowth during the formation of cubes was determined. Recall that the SnS cubes and spherical polyhedra are bound primarily by {011} planes, while the remaining facets of the cube (and some of the facets of the spherical polyhedra) display a diffraction pattern that is consistent with {h11} planes that are close to, but at a slightly deviated angle from, the (100) surface. Finally, exposed {010} and {001} facets are highly prominent in the spherical polyhedra, along with a smaller portion of {210} and {201} facets (Supporting Information, Figure S17), but these surfaces are absent in the cubes. Therefore, we suggest that the overgrowth process proceeds primarily in the ⟨010⟩ and ⟨001⟩ directions, and to a lesser extent in the ⟨210⟩ and ⟨201⟩ directions, and that the SnS spherical polyhedra can therefore be considered as truncated SnS cubes. The proposed structural model for the SnS cubes and spherical polyhedra is shown in Figure 8d,e. The SnS cubes are likely bound by {011} and {h11} facets, with the spherical polyhedra also displaying these along with {010}/{001} and smaller {210}/{201} facets.

Measurement of Optical Band Gaps of SnS Nanostructures. The band gaps of nanoscale semiconductors can deviate from their bulk counterparts due to quantum confinement effects.[56,57] Accordingly, Figure S18 (Supporting Information) shows the diffuse reflectance spectra acquired for the SnS cubes, spherical polyhedra, and sheets, which were drop-cast as films onto quartz substrates. In order to estimate and compare the optical band gaps (E_g), a Kubelka–Munk conversion was performed on the diffuse reflectance data, and plots of $[F(R)h\nu]^{1/2}$ vs $h\nu$ and $[F(R)h\nu]^2$ vs $h\nu$ were used to determine the indirect and direct band gaps, respectively. The E_g values were obtained by extrapolating the linear portion to the x-axis (Supporting Information, Figures S19–S21). The SnS nanosheets had indirect and direct band gaps of approximately 1.1 and 1.3 eV, respectively, which is consistent with previously reported values for bulk α-SnS.[5] In contrast, the measured indirect optical band gaps of the cubes and spherical polyhedra were 1.25 and 1.35 eV, respectively, and the direct band gaps were both close to 1.6 eV. This represents a blue shift with respect to bulk SnS by 0.15–0.25 eV for the indirect transition and 0.3 eV for the direct. The increase in E_g can be attributed to quantum confinement effects, since the exciton Bohr radius of bulk SnS is reported to be ~7 nm,[7] and this is also consistent with the increased band gaps reported previously for sub-10 nm SnS nanocrystals.[8,20] However, considering the similarity of their direct E_g values, the difference in indirect E_g values between the cubes and spherical polyhedra suggest that the optoelectronic properties of the as-deposited films may depend on the morphology and the accessible surfaces, as well as on the structural differences among the constituent particles. The Shockley–Queisser limit for maximum thermodynamic efficiency in semiconductor conversion of light into electrical free energy is achieved with a band gap of 1.1–1.4 eV,[58] a parameter which all of the SnS nanostructures fulfill. The UV–vis absorption spectra of the SnS cubes and spherical polyhedra are broad, with an onset starting at around 850–900 nm and extending throughout the visible region (Supporting Information, Figure S22). These properties make SnS nanocrystals a potentially attractive material for the bottom-up fabrication of optoelectronic devices.

Photocatalytic Degradation of Methylene Blue. Nanoscale semiconductors are well-known to photocatalytically degrade organic molecules, which can be applied toward environmental remediation.[59] Traditionally, wide-gap semiconductors such as TiO_2 are used with UV light;[60] however, narrow band gap semiconductors can utilize the longer wavelengths that comprise the majority of the solar spectrum.[61] Accordingly, we studied the activities of the SnS cubes, spherical polyhedra, and sheets for the visible light photodegradation of methylene blue (MB), which is a commonly used benchmark for photocatalytic treatment of molecular species (Figure 9). Repeated testing indicated that the SnS cubes were consistently more effective at MB degradation than the spherical polyhedra, and both were substantially more effective than the sheets. The higher surface area of the 0D nanocrystals compared to the sheets (based on their average sizes) results in significantly higher activities on a mass basis. However, although the SnS cubes and spherical polyhedra are approximately the same size with similar absorption spectra, the SnS cubes were found to degrade the MB nearly twice as fast. This behavior suggests shape-dependent photocatalytic activity, which has been demonstrated for other semiconductor nanocrystals[62] but, to our knowledge, not for SnS. The high proportion of exposed {011} planes on the SnS nanocubes implies that this facet is more active for the visible light photodegradation of MB than the {010} and {001} faces, by

dx.doi.org/10.1021/ja405203e | J. Am. Chem. Soc. 2013, 135, 11634–11644

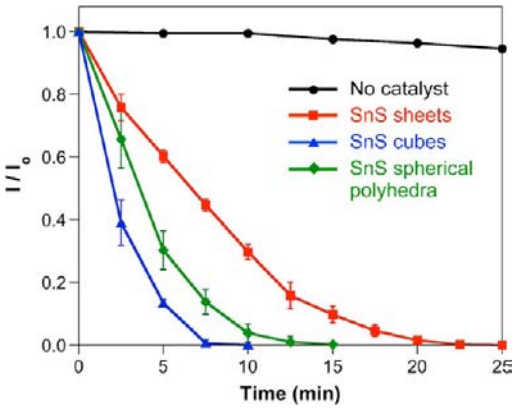

Figure 9. Determination of the activity of SnS sheets, cubes, and spherical polyhedra in the photocatalytic degradation of a known concentration of methylene blue by monitoring the decrease in absorbance at 663 nm relative to the initial absorbance (I/I_o) as a function of time.

which the spherical polyhedra are substantially bound. This may result from the repeating steps of atoms found on SnS{011} (Figure 6a), as uneven topology, and concomitantly undercoordinated surface atoms, often improves catalytic performance.[63] Additionally, complete degradation of MB is achieved substantially faster when using these nanocrystals compared to reports using other SnS nanomaterials, after normalization of reaction conditions, indicating their efficacy as viable and active photocatalysts.[12,15]

CONCLUSIONS

Given the emerging importance of SnS nanostructures in a diverse range of applications—including solar cells, field effect transitors, photodetectors, electrochemical capacitors, Li ion battery anodes, and photocatalysts—an in-depth understanding of fundamental aspects of their synthesis, crystal structure, and structure–property relationships is highly important. Accordingly, in this paper, we described the synthesis of colloidal SnS cubes, spherical polyhedra, and sheets, along with insights into how they form. Upon studying these diverse SnS nanostructures for the photocatalytic degradation of methylene blue—a benchmark reaction for photocatalysts—we gained insights into shape-dependent photocatalytic activity in the SnS system. The SnS cubes, which to our knowledge have not previously been reported, are particularly interesting because they form through seeded overgrowth of the spherical polyhedra and they have the highest photocatalytic activity for methylene blue degradation.

We also studied the shape-dependent polymorphism of the SnS cubes, spherical polyhedra, and sheets, given the direct impact that crystal structure has on properties. To do this, we used an in-depth crystallographic analysis of HRTEM/FFT data coupled with electron diffraction and powder XRD, an approach that offers a unique way of correlating diffraction data from both individual nanocrystals and ensembles of nanocrystals and therefore is likely to gain increasing utilization as unusual structural features continue to be observed in nanoscale solids. Specifically, these studies revealed that the experimentally observed diffraction patterns for the cubes and spherical polyhedra match significantly better with an alternate unit cell that is expanded along the *a* and *b* axes and contracted along *c*, converging on a pseudotetragonal cell that is measurably different from that of orthorhombic α-SnS, which is the most stable polymorph. This is important, because it helps to rationalize the discrepancies that exist between theoretical predictions of SnS polymorph stability, which indicate that ZB-type SnS is not likely to form, and experimental powder XRD data that have been interpreted to correspond to ZB-type SnS. Specifically, all of the peaks observed in powder XRD patterns that are frequently interpreted as originating from a mixture of ZB-type SnS and α-SnS can instead be accounted for by a single-phase pseudotetragonal modification of SnS, and this is also fully consistent with HRTEM and electron diffraction data of individual nanocrystals. As such, this study offers important insights not only into the polymorphism of the SnS system but also into the types of analyses that can lead to more reliable characterization of the crystal structures that nanoparticulate solids adopt.

ASSOCIATED CONTENT

Supporting Information

Additional characterization (EDS, nanobeam electron diffraction, TEM, HRTEM/FFT, UV–vis–NIR diffuse reflectance, UV–vis absorption), additional simulated X-ray and electron diffraction patterns, calculation of *d*-spacings and 2θ values, and Kubelka–Munk estimations of optical band gaps. This material is available free of charge via the Internet at http://pubs.acs.org.

AUTHOR INFORMATION

Corresponding Author

schaak@chem.psu.edu

Author Contributions

†These authors contributed equally.

Notes

The authors declare no competing financial interest.

ACKNOWLEDGMENTS

This work was supported primarily by the U.S. Department of Energy (DOE), Office of Basic Energy Sciences, Division of Materials Sciences and Engineering, under award #DE-FG02-08ER46483 (A.J.B., R.E.S.). D.D.V. acknowledges support from an NSF Graduate Research Fellowship. Electron microscopy was performed at the Electron Microscopy Facility at the Huck Institutes of the Life Sciences and at the Materials Characterization Lab of the Penn State Materials Research Institute. The authors thank Trevor Clark, Joseph Kulik, Xiaojun Weng, Ke Wang, and Josh Stapleton for their assistance with characterization and helpful discussions.

REFERENCES

(1) Brus, L. E. *J. Chem. Phys.* **1983**, *79*, 5566–5571.
(2) Schaller, R. D.; Klimov, V. I. *Phys. Rev. Lett.* **2004**, *92*, 186601.
(3) Talapin, D. V.; Lee, J.-S.; Kovalenko, M. V.; Shevchenko, E. V. *Chem. Rev.* **2010**, *110*, 389–458.
(4) Antunez, P. D.; Buckley, J. J.; Brutchey, R. L. *Nanoscale* **2011**, *3*, 2399–2411.
(5) Parenteau, M.; Carlone, C. *Phys. Rev. B* **1990**, *41*, 5227–5234.
(6) Ramasamy, K.; Kuznetsov, V. L.; Gopal, K.; Malik, M. A.; Raftery, J.; Edwards, P. P.; O'Brien, P. *Chem. Mater.* **2013**, *25*, 266–276.
(7) Yue, G. H.; Wang, L. S.; Wang, X.; Chen, Y. Z.; Peng, D. L. *Nanoscale Res. Lett.* **2009**, *4*, 359–363.
(8) Xu, Y.; Al-Salim, N.; Bumby, C. W.; Tilley, R. D. *J. Am. Chem. Soc.* **2009**, *131*, 15990–15991.
(9) Nozik, A. J. *Chem. Phys. Lett.* **2008**, *457*, 3–11.
(10) Sharon, M.; Basavaswaran, K. *Sol. Cells* **1988**, *25*, 97–107.
(11) Deng, Z.; Cao, D.; He, J.; Lin, S.; Lindsay, S. M.; Liu, Y. *ACS Nano* **2012**, *6*, 6197–6207.

(12) Chao, J.; Wang, Z.; Xu, X.; Xiang, Q.; Song, W.; Chen, G.; Hu, J.; Chen, D. *RSC Advances* **2013**, *3*, 2746−2753.
(13) Jayalakshmi, M.; Mohan Rao, M.; Choudary, B. M. *Electrochem. Commun.* **2004**, *6*, 1119−1122.
(14) Vaughn, D. D., II; Hentz, O. D.; Chen, S.; Wang, D.; Schaak, R. E. *Chem. Commun.* **2012**, *48*, 5608−5610.
(15) Chao, J.; Xie, Z.; Duan, X.; Dong, Y.; Wang, Z.; Xu, J.; Liang, B.; Shan, B.; Ye, J.; Chen, D.; Shen, G. *CrystEngComm* **2012**, *14*, 3163−3168.
(16) Albers, W.; Haas, C.; van der Maesen, F. *J. Phys. Chem. Solids* **1960**, *15*, 306−310.
(17) Walsh, A.; Watson, G. W. *J. Phys. Chem. B* **2005**, *109*, 18868−18875.
(18) Chamberlain, J. M.; Merdan, M. *J. Phys. C.: Solid State Phys* **1977**, *10*, L571−L574.
(19) Greyson, E. C.; Barton, J. E.; Odom, T. W. *Small* **2006**, *2*, 368−371.
(20) Hickey, S. G.; Waurisch, C.; Rellinghaus, B.; Eychmuller, A. *J. Am. Chem. Soc.* **2008**, *130*, 14978−14980.
(21) Deng, Z.; Han, D.; Liu, Y. *Nanoscale* **2011**, *3*, 4346−4351.
(22) Ning, J.; Men, K.; Xiao, G.; Wang, L.; Dai, Q.; Zou, B.; Liu, B.; Zou, G. *Nanoscale* **2010**, *2*, 1699−1703.
(23) Liu, H.; Liu, Y.; Wang, Z.; He, P. *Nanotechnology* **2010**, *21*, 105707.
(24) Zhang, H.; Hyun, B.-R.; Wise, F. W.; Robinson, R. D. *Nano Lett.* **2012**, *12*, 5856−5860.
(25) Avellaneda, D.; Nair, M. T. S.; Nair, P. K. *J. Electrochem. Soc.* **2008**, *155*, D517−D525.
(26) Gao, C.; Shen, H.; Wu, T.; Zhang, L.; Jiang, F. *J. Cryst. Growth* **2010**, *312*, 3009−3013.
(27) Gao, C.; Shen, H.; Sun, L.; Shen, Z. *Mater. Lett.* **2011**, *65*, 1413−1415.
(28) Ren, L.; Jin, Z.; Wang, W.; Liu, H.; Lai, J.; Yang, J.; Hong, Z. *Appl. Surf. Sci.* **2011**, *258*, 1353−1358.
(29) Lu, J.; Nan, C.; Li, L.; Peng, Q.; Li, Y. *Nano Res.* **2013**, *6*, 55−64.
(30) Burton, L. A.; Walsh, A. *J. Phys. Chem. C* **2012**, *116*, 24262−24267.
(31) Kaminsky, W. *J. Appl. Crystallogr.* **2005**, *38*, 566−567.
(32) Liu, J.; Xue, D. *Electrochim. Acta* **2010**, *56*, 243−250.
(33) Aso, K.; Hayashi, A.; Tatsumisago, M. *Cryst. Growth Des.* **2011**, *11*, 3900−3904.
(34) Zhang, Y.; Lu, J.; Shen, S.; Xu, H.; Wang, Q. *Chem. Commun.* **2011**, *47*, 5226−5228.
(35) Vaughn, D. D., II; Patel, R. J.; Hickner, M. A.; Schaak, R. E. *J. Am. Chem. Soc.* **2010**, *132*, 15170−15172.
(36) Vaughn, D. D., II; In, S.-I.; Schaak, R. E. *ACS Nano* **2011**, *5*, 8852−8860.
(37) Villars, P. *Pearson's Handbook Desk Edition: Crystallographic Data for Intermetallic Phases*; ASM International: Materials Park, OH, 1998.
(38) Baumgardner, W. J.; Choi, J. J.; Lim, Y.-F.; Hanrath, T. *J. Am. Chem. Soc.* **2010**, *132*, 9519−9521.
(39) Radovsky, G.; Popovitz-Biro, R.; Tenne, R. *Chem. Mater.* **2012**, *24*, 3004−3015.
(40) Xia, T.; Chen, X. *J. Mater. Chem. A* **2013**, *1*, 2983−2989.
(41) Lambert, K.; Geyter, B. D.; Moreels, I.; Hens, Z. *Chem. Mater.* **2009**, *21*, 778−780.
(42) Sharma, R. C.; Chang, Y. A. *Bull. Alloy Phase Diagr.* **1986**, *7*, 269−273.
(43) von Schnering, H. G.; Wiedemeir, H. *Z. Kristallogr.* **1981**, *156*, 143−150.
(44) Ehm, L.; Knorr, K.; Dera, P.; Krimmel, A.; Bouvier, P.; Mezouar, M. *J. Phys.: Condens. Matter* **2004**, *16*, 3545.
(45) Brownson, J. R. S.; Georges, C.; Levy-Clement, C. *Chem. Mater.* **2006**, *18*, 6397−6402.
(46) Mariano, A. N.; Chopra, K. L. *Appl. Phys. Lett.* **1967**, *10*, 282−284.
(47) Bilenkii, B. F.; Mikolaichuk, A. G.; Freik, D. M. *Phys. Status Solidi* **1968**, *28*, K5−K7.
(48) Badachhape, S. B.; Goswami, A. *J. Phys. Soc. Jpn.* **1962**, *17* (Suppl. B-II), 251−253.
(49) Koktysh, D. S.; McBride, J. R.; Geil, R. D.; Schmidt, B. W.; Rogers, B. R.; Rosenthal, S. J. *Mater. Sci. Eng., B* **2010**, *170*, 117−122.
(50) de Kergommeaux, A.; Faure-Vincent, J. r. m.; Pron, A.; de Bettignies, R. m.; Malaman, B.; Reiss, P. *J. Am. Chem. Soc.* **2012**, *134*, 11659−11666.
(51) Chen, C.-C.; Herhold, A. B.; Johnson, C. S.; Alivisatos, A. P. *Science* **1997**, *276*, 398−401.
(52) Biacchi, A. J.; Schaak, R. E. *ACS Nano* **2011**, *5*, 8089−8099.
(53) Jana, N. R.; Gearheart, L.; Murphy, C. J. *Chem. Mater.* **2001**, *13*, 2313−2322.
(54) DeSantis, C. J.; Sue, A. C.; Bower, M. M.; Skrabalak, S. E. *ACS Nano* **2012**, *6*, 2617−2628.
(55) Pietryga, J. M.; Schaller, R. D.; Werder, D.; Stewart, M. H.; Klimov, V. I.; Hollingsworth, J. A. *J. Am. Chem. Soc.* **2004**, *126*, 11752−11753.
(56) Smith, A. M.; Nie, S. *Acc. Chem. Res.* **2009**, *43*, 190−200.
(57) Banerjee, R.; Jayakrishnan, R.; Ayyub, P. *J. Phys.: Condens. Matter* **2000**, *12*, 10647.
(58) Shockley, W.; Queisser, H. J. *J. Appl. Phys.* **1961**, *32*, 510−519.
(59) Asahi, R.; Morikawa, T.; Ohwaki, T.; Aoki, K.; Taga, Y. *Science* **2001**, *293*, 269−271.
(60) Ollis, D. F.; Pelizzetti, E.; Serpone, N. *Environ. Sci. Technol.* **1991**, *25*, 1522−1529.
(61) Zhang, Y. C.; Du, Z. N.; Li, K. W.; Zhang, M. *Sep. Purif. Technol.* **2011**, *81*, 101−107.
(62) Gordon, T. R.; Cargnello, M.; Paik, T.; Mangolini, F.; Weber, R. T.; Fornasiero, P.; Murray, C. B. *J. Am. Chem. Soc.* **2012**, *134*, 6751−6761.
(63) Lee, I.; Delbecq, F.; Morales, R.; Albiter, M. A.; Zaera, F. *Nat. Mater.* **2009**, *8*, 132−138.